# Toward Relating Open- and Closed-Test Section Microphone Phased Array Aeroacoustic Measurements

Christopher J. Bahr*

*NASA Langley Research Center, Hampton, Virginia, 23681*

**Aeroacoustic measurements utilizing microphone phased arrays are becoming more commonplace in large-scale wind tunnels. However, for such costly tests, it is difficult to assess the influence of a given facility's configuration on the acquired data. One such opportunity has recently arisen in the NASA Langley Research Center 14- by 22-Foot Subsonic Tunnel, where the High-Lift configuration of the Common Research Model was tested in both open-jet and closed wall (or test section) configurations. Acoustic data were acquired on the same model with the same specific hardware at the same Mach number; and for similar model angles of attack, array apertures, and array angles relative to the model location. Initial deconvolution comparisons using DAMAS appear poor. The closed test section results show contamination likely due to background noise and reflections. The open-jet results show severe blurring due to the decorrelation of acoustic waves passing through a turbulent free shear layer. However, accounting for image sources in the DAMAS grid reduces visual artifacts in the closed test section results, and a preliminary coherence correction technique mitigates the blurring in the open-jet results. Qualitatively, both tests identify similar source behavior. Quantitatively, summed spectra of the slat noise agree in some frequency bands but differ in others. Proposals that may mitigate the difference are given for each configuration, such as correcting for the array protective cover and applying background subtraction in the closed wall configuration, and further developing the coherence loss correction for deconvolution methods in the open-jet setup.**

## I. Introduction

AEROACOUSTIC measurements in wind tunnel testing are an important part of the development of many technologies and products in aeronautics. Various factors may drive the choice of facility configuration for a given test. Historically, open-jet wind tunnel tests have been preferred for aeroacoustic measurements, though more recently hybrid facilities have been proposed with similar benefits [1, 2]. Both of these configurations remove acoustic instrumentation from the (primary) wind tunnel flow field, mitigating hydrodynamic pressure fluctuation contamination of acoustic measurements. Additionally, they allow for the acoustic treatment of the wind tunnel test section to, in ideal circumstances, approach an anechoic condition. However, open-jet testing generally comes with an aerodynamic penalty for high-lift configurations. Also, it introduces a turbulent free shear layer that scatters acoustic waves. This can have a limiting effect on microphone array measurements [3]. Hybrid tunnel testing mitigates these effects at the expense of increased tunnel background noise [4], but is currently limited to a select few facilities around the world.

Closed wall aerodynamic wind tunnels, while not preferred for purely acoustic measurements, have some benefits when choosing to conduct an aeroacoustic test. One of the main factors may be cost, as combining aerodynamic and aeroacoustic measurement campaigns is a major way to reduce testing expense in large wind tunnel facilities. Additionally, some unique facility capabilities are limited to closed test section configurations with no acoustic treatment [5]. However, in many cases, the tunnel walls are approximately rigid in the acoustic sense, leading to significant reflections in the reverberant environment. These reflections can significantly complicate acoustic signal analysis.

Microphone phased arrays are used in both open-jet and closed wall wind tunnel configurations to identify noise sources and to attempt to determine source levels. It is well documented that conventional beamforming suffers reduced performance in reverberant facilities with both reduced resolution [6, 7] and greater variability in level estimates [8, 9] when compared to the free field. These difficulties also carry over to a lesser extent with deconvolution methods, such as DAMAS [10]. However, open-jet facilities are also not truly free field equivalents due to the reasons cited above. The broad objective of universally correcting microphone phased array measurements to an ideal free field is an extremely

---

difficult topic and beyond the capability of any one paper to address. However, a subset of questions can be posed. How much variability in array results exists between facility configurations for a given model under similar operating conditions, and can this variability be reduced? Using physics-based corrections to bring acoustic measurements into agreement for a given model in different facility configurations, each with their own limitations, may be a significant step toward reducing the limitations of microphone phased arrays in the analysis of complex noise sources in large-scale wind tunnels. Such studies have been conducted before using conventional beamforming [11], but it is a worthwhile effort to revisit such research with deconvolution routines and increased computing power.

Recently, an opportunity to study these questions has arisen from a pair of tests that have been conducted in the NASA Langley Research Center 14- by 22-Foot Subsonic Tunnel (14x22). In these tests, the high-lift version of the Common Research Model (CRM-HL) underwent extensive analysis in both the closed and open-jet configurations of the 14x22. For a subset of these tests, the model high-lift rigging was matched and acoustic measurements were taken at similar aerodynamic operating conditions in both tunnel configurations [12]. This work presents a preliminary comparison of the microphone phased array measurements from each test. It does so by first analyzing the data using the baseline Deconvolution Approach for the Mapping of Acoustic Sources (DAMAS) algorithm [13]. It then evaluates how each facility configuration violates the original DAMAS model, and how DAMAS might be corrected. The modified DAMAS results are then computed and compared. Remaining limitations in the corrections are discussed, with further improvements proposed.

## II. Formulation Review

As this work involves possible modifications to the DAMAS algorithm, it is worth reviewing the initial problem formulation. This requires a brief overview of the conventional beamformer.

### A. Conventional beamforming

For conventional beamforming in the frequency domain, an array of $N$ microphones measures an acoustic field. A source $q$ is assumed to exist at location $\ell$. A Green's function $g$ is chosen as an assumed model for propagation, such that for a given frequency, the column vector of microphone measurements is given by

$$\mathbf{p} = \mathbf{g}_\ell q_\ell. \tag{1}$$

To aim or steer the array to a point in space $\ell'$, a function $h$ is chosen. The column vector to steer the microphone data to $\ell'$ is thus $\mathbf{h}_{\ell'}$. The beamforming output $b$ at $\ell'$ due to a source at $\ell$ is thus given by

$$b_{\ell'} = \mathbf{h}_{\ell'}^\dagger \mathbf{p} = \mathbf{h}_{\ell'}^\dagger \mathbf{g}_\ell q_\ell, \tag{2}$$

with superscript $\dagger$ denoting the Hermitian transpose of a vector or matrix. For most aeroacoustic applications, the ensemble average of the beamforming output is actually computed by using the averaged cross-spectral matrix $\mathbf{C}$ and assuming deterministic propagation [14],

$$B_{\ell'} = \left\langle b_{\ell'} b_{\ell'}^* \right\rangle = \mathbf{h}_{\ell'}^\dagger \left\langle \mathbf{p}\mathbf{p}^\dagger \right\rangle \mathbf{h}_{\ell'} = \mathbf{h}_{\ell'}^\dagger \mathbf{C}\mathbf{h}_{\ell'}, \tag{3}$$

with superscript $*$ denoting the complex conjugate of a scalar.

### B. Green's functions

For conventional beamforming, the starting point for modeling propagation is usually the free space Green's function. In the frequency domain, this is given by the solution to the Helmholtz equation as [14]

$$g_{n,\ell} = \frac{1}{4\pi r_{n,\ell}} e^{-jkr_{n,\ell}}, \tag{4}$$

where $k$ is the angular acoustic wavenumber

$$k = \frac{2\pi f}{c_0}, \tag{5}$$

$r$ the distance from source $\ell$ to microphone $n$

$$r_{n,\ell} = \sqrt{(x_n - x_\ell)^2 + (y_n - y_\ell)^2 + (z_n - z_\ell)^2}, \tag{6}$$

2

and $c_0$ the isentropic speed of sound. The original DAMAS algorithm incorporates Amiet's shear layer refraction model to provide magnitude and phase corrections to $g_{n,\ell}$ when testing in an open-jet wind tunnel. Beamforming in a closed wall wind tunnel can be accomplished by modeling the flow as infinite and using the Green's function for the convective Helmholtz equation [15].

### C. Steering vectors

Steering vector $h$ is usually chosen such that it matches certain characteristics for $\ell' = \ell$. Sarradj identifies four formulations, which are commonly used in aeroacoustics for beamforming with microphone phased arrays [16]. These are repeated here, and adjusted to allow for nonuniform microphone weighting or array shading. With array shading, individual microphone weights $w$ are applied to alter the response of an array to achieve some desired trait [17].

The first steering vector formulation is an element-by-element phase compensation for the microphones in the array. Each element of the steering vector is given by

$$h^{\mathrm{I}}_{n,\ell'} = \frac{w_n}{\sum_{n'=1}^{N} w_{n'}} \frac{g_{n,\ell'}}{\left| g_{n,\ell'} \right|}. \tag{7}$$

The second formulation adds an element-by-element amplitude compensation. Each element of the steering vector is given by

$$h^{\mathrm{II}}_{n,\ell'} = \frac{w_n}{\sum_{n'=1}^{N} w_{n'}} \frac{g_{n,\ell'}}{\left| g_{n,\ell'} \right|^2}. \tag{8}$$

The third formulation provides a distortionless filter when the array is steered to the correct source location. This steering vector takes the form

$$\mathbf{h}^{\mathrm{III}}_{\ell'} = \frac{\mathbf{W}^2 \mathbf{g}_{\ell'}}{\mathbf{g}_{\ell'}{}^{\dagger} \mathbf{W}^2 \mathbf{g}_{\ell'}}, \tag{9}$$

where $\mathbf{W}$ is a diagonal matrix of the microphone weighting values. The fourth formulation applies a normalization to keep the steering vector magnitude constant, while keeping the steering vector parallel to the propagation vector when the array is steered to the correct source location. This vector takes the form

$$\mathbf{h}^{\mathrm{IV}}_{\ell'} = \frac{\mathbf{W}}{\sqrt{\sum_{n'=1}^{N} \left( w_{n'}^2 \right)}} \frac{\mathbf{W} \mathbf{g}_{\ell'}}{\sqrt{\mathbf{g}_{\ell'}{}^{\dagger} \mathbf{W}^2 \mathbf{g}_{\ell'}}}. \tag{10}$$

If shading is not used, $w_n = 1$ for all $n$, and these equations revert to those given in the reference. These formulations incorporate all stages of array shading, so Eq. (3) does not change, unlike in other references. Note that diagonal removal [18] significantly alters these formulations, and is not addressed here. In this work, formulation IV is used, as it yields a beamforming maximum at the true source location [16] and thus should generate a DAMAS coefficient matrix with maxima along the diagonal.

### D. DAMAS

The conventional beamforming output $b$ is strongly influenced by the characteristics of a given array design. DAMAS is a deconvolution technique that attempts to remove this influence through further modeling and a constrained Gauss-Seidel solution to the resultant ill-conditioned system of equations [13]. For conventional usage, it assumes all sources are mutually incoherent point sources.

The DAMAS system is formulated as

$$\mathbf{b} = \mathbf{A}\mathbf{q}, \tag{11}$$

where $\mathbf{b}$ and $\mathbf{q}$ are the respective column vectors of beamforming outputs $B$ and ensemble-averaged source powers $Q = \langle qq^* \rangle$ for a grid of $L$ candidate sources. Matrix $\mathbf{A}$ is the system matrix for this problem, where columns of $\mathbf{A}$ represent the point spread function of the array for a given source location. Elements of the matrix are computed as

$$A_{\ell',\ell} = \left( \mathbf{h}^{\dagger}_{\ell'} \mathbf{g}_{\ell} \right) \left( \mathbf{h}^{\dagger}_{\ell'} \mathbf{g}_{\ell} \right)^*. \tag{12}$$

This statement can be simplified by arranging propagation vectors $\mathbf{g}$ and steering vectors $\mathbf{h}$ into $N \times L$ sized matrices $\mathbf{G}$ and $\mathbf{H}$, and computationally accelerated by solving

$$\mathbf{A} = \left( \mathbf{H}^{\dagger} \mathbf{G} \right) \odot \left( \mathbf{H}^{\dagger} \mathbf{G} \right)^*, \tag{13}$$

3

where operator $\odot$ denotes the Hadamard product of two matrices. As with the steering vector formulations, applying diagonal removal greatly complicates this formulation and is not addressed here.

DAMAS solves for $\mathbf{q}$ using the Gauss-Seidel algorithm, where at each step, the source level is constrained to $Q_\ell \geq 0$. The order in which the sources are evaluated has been found to influence the output of DAMAS [19]. In this work, two-dimensional scan planes are evaluated using alternating directions on four orderings of points, two column-major and two row-major. This appears to minimize the sweeping of energy through source points that can otherwise occur.

## III. DAMAS Modifications

The DAMAS review above is the starting point for tailoring the deconvolution algorithm to account for facility-specific characteristics, beyond accounting for mean flow or shear layer refraction.

### A. Closed test sections - reverberance and image sources

When perfectly reflecting surfaces are present in a closed test section, the propagation formulation used in DAMAS can be modified to account for the presence of image sources. These take the form of image sources at locations $i$,

$$g_{I,n,\ell} = \frac{1}{4\pi r_{n,\ell}}e^{-jkr_{n,\ell}} + \sum_{i=1}^{I}\frac{1}{4\pi r_{n,i}}e^{-jkr_{n,i}} = g_{n,\ell} + \sum_{i=1}^{I}g_{n,i}. \tag{14}$$

It can be further modified to account for partial absorption of reflections, but such effects are not considered here.

This Green's function modification has been used in some prior studies to construct steering vectors used in conventional beamforming [6–9]. It yielded mixed results in some cases. More recent work suggests that, at least with DAMAS, accurate models of propagation should be incorporated into the Green's function selection for construction of Matrix $\mathbf{A}$, but that the steering vectors should still be formulated with free-space propagation (still selected with the appropriate flow model to allow for accurate qualitative source localization) [10]. This observation is advantageous in that it allows for full correction of realistic propagation effects in more efficient, non-DAMAS-based deconvolution formulations [20].

The above modifications hold for deterministic propagation environments, where the image of an acoustic source maintains perfect coherence with the true source. However, wind tunnel testing is rarely so clean, and several factors, such as finite correlation timescales of sources, propagation through wall boundary layers, and data processing choices, can all decorrelate an image from the true source. When the image completely decorrelates, there are at least two ways to directly incorporate reflections into DAMAS. The first is to maintain the original DAMAS Green's function selection and extend the deconvolution grid to capture image sources. This has computational drawbacks due to an increase in grid size, but allows for analysis using existing codes. The second is to modify the propagation model used in the DAMAS coefficient matrix separately from the Green's function selection. Conceptually, Eq. (12) can be viewed as beamforming on a rank 1 CSM normalized to isolate propagation characteristics from the acoustic source. Its use can be expressed alternately using Eq. (3) as

$$B_{\ell'} = \mathbf{h}_{\ell'}^{\dagger}\mathbf{C}_\ell\mathbf{h}_{\ell'} = \mathbf{h}_{\ell'}^{\dagger}\left(\mathbf{g}_\ell\mathbf{g}_\ell^{\dagger}\right)\mathbf{h}_{\ell'}Q_\ell = A_{\ell',\ell}Q_\ell, \tag{15}$$

where the normalized CSM is given by $\mathbf{g}_\ell\mathbf{g}_\ell^{\dagger}$ and models deterministic, free field propagation. This can be modified to account for uncorrelated image sources by substituting a CSM that additively incorporates them,

$$\mathbf{C}_{I,\ell} = \mathbf{C}_\ell + \sum_{i=1}^{I}\mathbf{C}_i. \tag{16}$$

The substitution yields an equation for the elements of the coefficient matrix,

$$A_{d,\ell',\ell} = \mathbf{h}_{\ell'}^{\dagger}\left(\mathbf{g}_\ell\mathbf{g}_\ell^{\dagger} + \sum_{i=1}^{I}\mathbf{g}_i\mathbf{g}_i^{\dagger}\right)\mathbf{h}_{\ell'}. \tag{17}$$

Note that the computational savings realized with Eq. (13) are reduced in the formulation of Eq. (17). However, these losses can be partially mitigated through creative code factorization and the leveraging of GPU computing resources.

Compensating for partial decorrelation requires either a knowledge-based blending of Eqs. (14) and (17) or deconvolution techniques that allow for arbitrary source coherence. Such analysis is beyond the scope of this work.

**B. Open-jet test sections - coherence loss**

Coherence loss is one term used to describe the frequency domain behavior of an acoustic signal that passes through a random medium and is measured by multiple observers. When a wave propagates through turbulence, it is scattered. This scattering can be modeled in the frequency domain as randomized magnitude and phase fluctuations [21]. These fluctuations reduce the computed covariance of pressures measured at different observers. The reduction is a function of frequency, sensor separation, propagation path, and turbulence characteristics [3, 22]. The end result of this reduction is that the computed coherence between two observers is less than it should be. Mathematically, this can be modeled as

$$\mathbf{C}_d = \mathbf{C} \odot \mathbf{\Gamma}, \tag{18}$$

where subscript $d$ denotes decorrelation and $\mathbf{\Gamma}$ is the matrix that models coherence loss, or the mutual coherence function (MCF). This effect has been demonstrated repeatedly in open-jet wind tunnels [4, 23–25].

DAMAS (and other deconvolution routines) can be modified to account for coherence loss by incorporating the effect into the acoustic propagation model. Incorporating propagation through turbulence is accomplished by substituting a CSM that accounts for coherence loss

$$\mathbf{C}_{d,\ell} = \mathbf{C}_\ell \odot \mathbf{\Gamma}_\ell, \tag{19}$$

yielding an equation for the elements of the coefficient matrix as

$$A_{d,\ell',\ell} = \mathbf{h}_{\ell'}^\dagger \left[ \left( \mathbf{g}_\ell \mathbf{g}_\ell^\dagger \right) \odot \mathbf{\Gamma}_\ell \right] \mathbf{h}_{\ell'}. \tag{20}$$

As long as the MCF can be modeled for a given installation, DAMAS can thus be modified to account for decorrelation. As with Eq. (17), Eq. (20) is more computationally expensive than Eq. (13). Again some savings may be realized through creative code design and GPU utilization. Note that in extreme scattering circumstances where $\mathbf{\Gamma}_\ell$ approaches a purely diagonal matrix, it is expected that DAMAS, and for that matter any other phased array analysis routine, will fail, as no cross-spectral information is available for localization.

# IV. Test Description

Acoustic data were acquired on the CRM-HL in the 14x22 for a closed wall configuration in 2018 [26] and for an open-jet configuration in 2020/2021 [12]. An overview of each test can be found in the respective references. As the acoustic portion of the 2018 test was short, very few configurations were studied. The baseline configurations that were measured were duplicated for a portion of the 2020/2021 test. The same model settings were tested at the same test section Mach number. Angles of attack (AoA) were slightly different to closely match mean pressure distributions, such that for this comparison, the 7° AoA data from the closed wall test are shown against the 8.5° AoA data from the open-jet test. For the most part, these are in excellent agreement. In this work, the data acquired for the full-span slat (FSS) are considered at Mach numbers of 0.16 and 0.2, although common data for the part-span slat (PSS) are available as well.

The array used in the closed wall test consisted of 110 1/4-inch microphones, and is shown in Fig. 1. The overall diameter of the array pattern was 1.83 m, with an innermost ring diameter of 5.08 cm. The array face, slightly offset from the tunnel wall, was located 1.78 m off the floor, 22.3 cm upstream of the center of the model turntable, and 3.33 m from the center of the model turntable in the remaining flow-normal direction. A screen cover was installed over the array face for part of the test. This cover, consisting of a fine screen mesh overlaying a perforate steel sheet, offset the facility wall boundary layer from the array microphones and significantly improved the signal-to-noise ratio of the measurements. In this work, only data acquired using the array's protective cover are processed, as the signal-to-noise ratio in the measurements was poor without it. The influence of this cover on the array output is not incorporated in the processing. Other work suggests that a similar screen might require adjustments on the order of one or two dB as a function of frequency and angle of incidence [27], both due to screen transmission loss and a minor standing wave pattern between the cover and microphone plate. The perforate steel sheet likely increases the magnitude of this adjustment factor. For this test, empty tunnel background noise data were not acquired.

The array used in the open-jet test consisted of 97 1/4-inch microphones, and is shown with the CRM-HL in Fig. 2. This array had been designed for previous open-jet tests in the 14x22 [28]. The overall diameter of the array pattern was 2.00 m, with an innermost ring diameter of 3.85 cm. The array face was located 1.83 m off the floor, 5.17 m from the center of the model turntable in the remaining flow-normal direction, and could traverse along the length of the test section in the flow direction. For this installation, the array face had no protective cover. In this work, all data considered are for the array at its 90° station, corresponding to the streamwise position of the model turntable. The acoustic treatments shown in the figure are discussed in companion work [12]. For this test, empty tunnel background noise data were acquired.
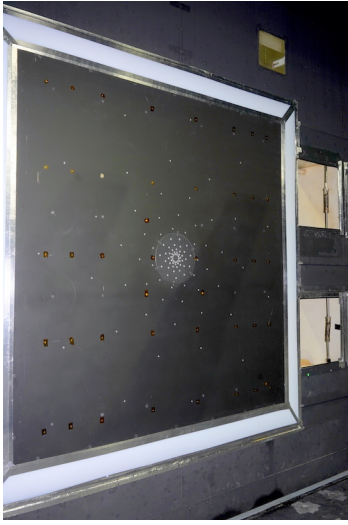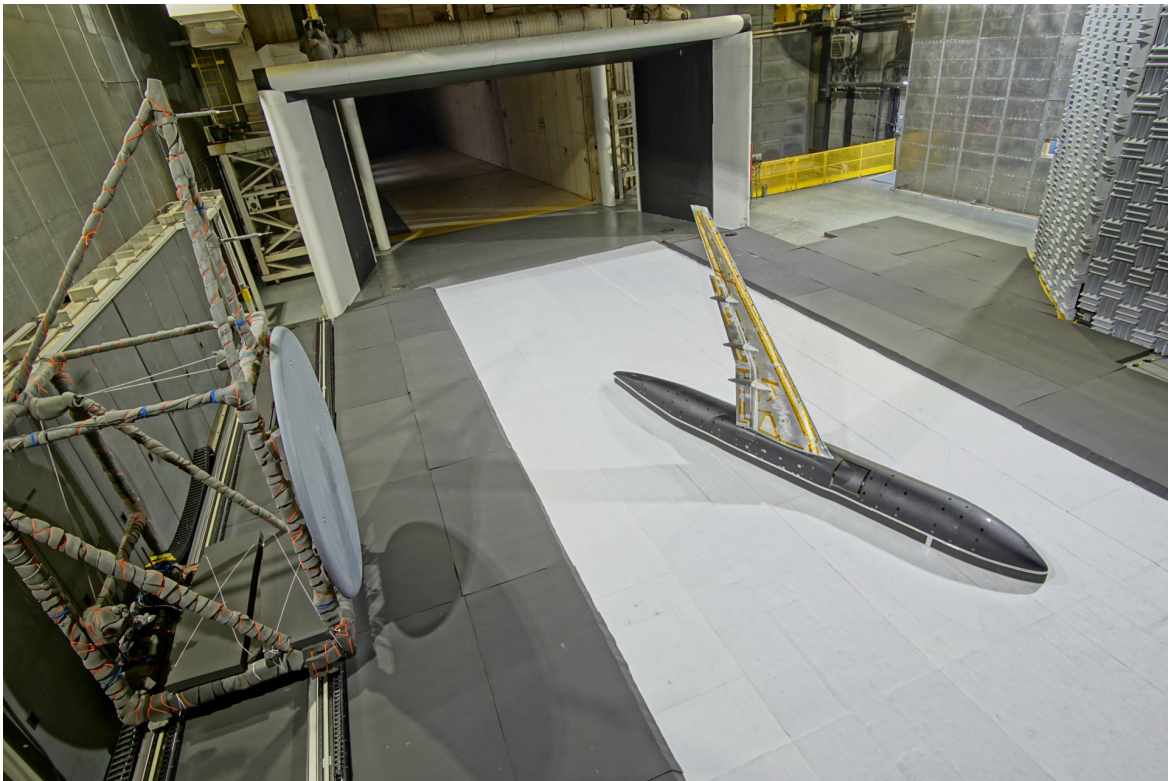
(a)                                                                                      (b)

**Fig. 1     Microphone array installed on the wall of the 14x22 closed test section, shown (a) as a bare plate and (b) with a protective screen and with the CRM-HL.**



**Fig. 2     Traversing microphone array and CRM-HL model in the open-jet configuration of the 14x22.**

# V. Data Processing

Acoustic data were recorded using the same system in both tests. Bandpass filter settings were not matched between the tests, but the 2 kHz to 40 kHz range considered in this work was within the passband for both. Data were acquired at a sampling rate of 196,608 samples/sec for 35 seconds. Spectra are computed using block lengths of 2,048 samples, yielding a narrowband binwidth of 96 Hz. Blocks are processed with a Hann window and 75% overlap.

## A. Conventional beamforming and baseline DAMAS

Array analysis routines are applied to the CSMs generated using these parameters. For the closed test section data from 2018, the diagonal optimization technique described by Hald [29] is used to reduce flow noise since no empty tunnel data are available. This method mitigates uncorrelated noise contamination along the CSM diagonal while maintaining its positive semidefinite behavior, in contrast with diagonal removal. For the open-jet test section data, subspace-based background subtraction is used [30].

DAMAS requires conventional beamforming as an input. As mentioned previously, the steering vector formulation from Eq. (10) is used in all beamforming calculations here. Steering vectors are constructed from the free field Green's function for the convective Helmholtz equation for the closed wall test, and from the free field Green's function for the Helmholtz equation with Amiet's magnitude and delay corrections for the open-jet test [31]. An array shading scheme is optimized to hold both array responses to a 22.5 cm 3-dB beamwidth across the majority of their operational bandwidth, with a controlled increase in beamwidth at lower frequencies [32]. Matching the beamwidth relaxes grid spacing requirements so that a common grid for both datasets can be used. The grid is selected to encompass the wing section of the model, spanning approximately 4 m in the streamwise direction and 5 m in the flow normal direction, with 1 m extended into the floor to capture noise sources that appeared on the floor for portions of the open-jet test [12]. The grid point spacing is 4.5 cm, yielding 5 points per beamwidth and 10,080 grid points. There is one exception to this grid definition, discussed further below. For all cases, the grid is rotated to match the model dihedral and AoA.

For all DAMAS calculations, the propagation models used in the construction of the coefficient matrix incorporate atmospheric attenuation to estimate lossless deconvolution output [33]. A microphone directivity correction is also applied [34] , though the directivity correction is small for the considered incidence angles and frequencies. The DAMAS algorithm itself is applied using 200 forward-backward iterations following four different grid traversing orders. Appropriate scaling is required to compare quantitative results between the tests, as the existing codes scale source strengths to the center of the respective array for each test. This is done by losslessly depropagating the calculated level of each grid point from the closed wall test to unit distance using the convective Helmholtz equation Green's function, and repropagating the results to the coordinates of the array center from the open-jet test using the Helmholtz equation Green's function. No scaling of the open-jet data is performed, as Amiet's method corrects for an emission distance equal to the physical source-to-array distance. The resulting grid values are subsequently reduced by 6 dB to account for pressure doubling on each array face. Finally, they are summed within desired regions to estimate source levels. These regions are shown in Fig. 3.

Note that this scaling does not capture every effect necessary to collapse the data. First, the array locations, while close in the streamwise angular sense, do not match. Highly directive sources that do not change between the closed wall and open-jet configurations may be seen differently. Second, the array in the closed wall test, being closer to the model, may experience some nearfield effects, which dissipate by the time they would reach the open-jet array.

## B. Configuration-specific propagation model adjustments

To compare the baseline DAMAS analysis to facility-specific propagation corrections, certain choices must be made. For the closed wall test, it must be decided whether to treat the reflections in the facility as coherent or incoherent. Cross-beamforming can be used to assess this behavior [35]. In cross-beamforming, the cross-spectrum of every point in a grid referenced to a single point is computed, rather than the autospectral level of every grid point. Computing both cross-spectra and autospectra for every grid point allows for the calculation of a coherence between all the points in a given beamforming grid and a reference point. It should be noted that this is a highly qualitative comparison due to previous caveats and the complexity of coherence analysis for multipath, multi-input/multi-output signals. However, it may be reasonable to use cross-beamforming to inform processing choices. It is probably not reasonable to trust it as a quantitative statement of coherence values.

The cross-beamforming coherence output for a slat grid point at two different frequencies is shown in Fig. 4. Note that this plot was processed for earlier research [10] and uses a different shading scheme and grid than the rest of the analysis presented in this manuscript. The coherence maps show that for a slat tone frequency (a), there are significant
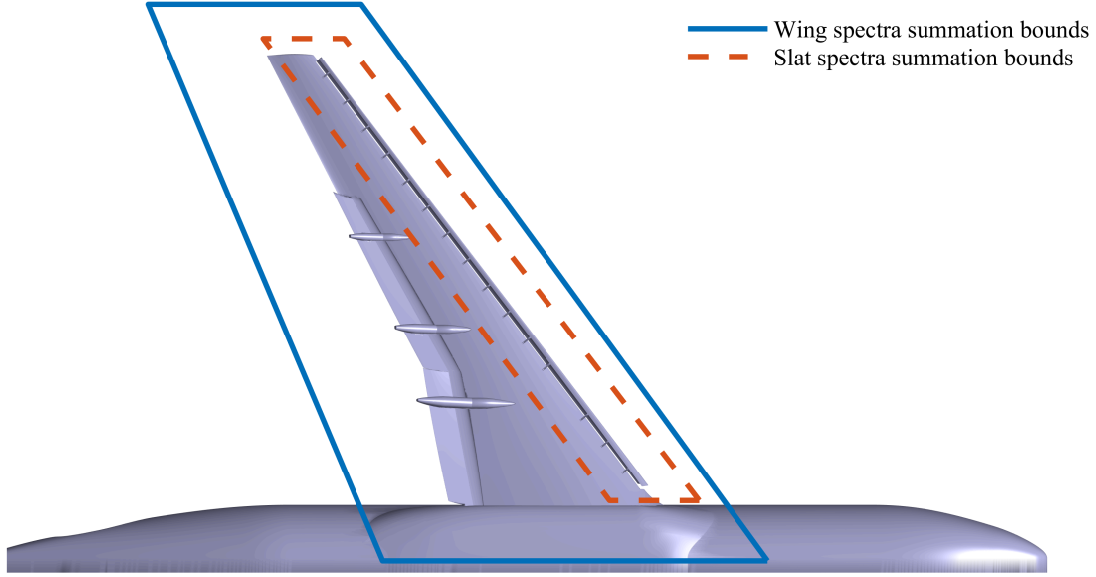
**Fig. 3    Overlay of summed spectra regions with the CRM-HL model.**

high-coherence estimates. The floor reflection falls onto one of these, though most of the lobes in the map are strong. The ceiling reflection, for some reason, shows low coherence. For a broadband frequency (b), there is very little coherence seen for frequencies outside of the conventional beamforming mainlobe. These results suggest that the slat tone image sources may be coherent, and the broadband may be incoherent. As mixed-coherence analysis is outside the scope of this work and slat tones are considered a model scale artifact [12], the image sources are treated as incoherent. To utilize the existing code, this is done by constructing a beamforming grid that captures the primary reflection images rather than by modifying the DAMAS propagation matrix. The resultant grid discards the bottom meter of the baseline grid but then reflects it across the floor and ceiling, yielding a final grid size of 24,030 points.

For the open-jet test, an appropriate estimate of $\mathbf{\Gamma}_\ell$ must be constructed. Unsteady flow measurements of the facility free shear layer with the CRM-HL installed are unavailable. However, the CRM-HL has speakers embedded in the wing. For a speaker signal emanating from location $\ell$ that dominates airframe and facility noise and has only one significant propagation path, $\mathbf{\Gamma}_\ell$ is straightforward to measure [25]. Under such conditions with deterministic propagation, a measured CSM ought to yield a coherence of one. The as-measured coherence is thus representative of $\mathbf{\Gamma}_\ell$. However, the measured coherence needs to be generalized to other grid points and possibly to off-design operating conditions.

Generalizing $\mathbf{\Gamma}_\ell$ to $\mathbf{\Gamma}$ can be accomplished by fitting the measurement to a model of the MCF [22]. Wilson gives the MCF as

$$\gamma\left(\rho\right) = \exp\left\{-\frac{\pi k^2 \mathcal{X}}{2}\left[b_c\left(0\right) - b_c\left(\rho\right)\right]\right\}, \tag{21}$$

where $\gamma$ is an individual element of matrix $\mathbf{\Gamma}$, $\rho$ is the separation between two observers, $\mathcal{X}$ is the propagation distance through the turbulent medium, and $b_c$ is a 2-D correlation function. $\mathcal{X}$ can be estimated from Amiet-based propagation path calculations projected through historical (unpublished) measurements of the 14x22 open-jet free shear layer. The correlation function $b_c$ is selected from several given by Wilson. For data acquired in the CRM-HL test, the von Kármán correlation function provides the best fit. This function is given by

$$b_c\left(\rho\right) = \frac{4\sigma^2\mathcal{L}}{3\sqrt{\pi}\Gamma\left(\frac{1}{3}\right)}\left(\frac{\rho}{2\mathcal{L}}\right)^{\frac{5}{6}}\left[K_{\frac{5}{6}}\left(\frac{\rho}{\mathcal{L}}\right) - \frac{\rho}{2\mathcal{L}}K_{\frac{1}{6}}\left(\frac{\rho}{\mathcal{L}}\right)\right]. \tag{22}$$

Note that $\Gamma$ is the Gamma function, as opposed to the boldfont $\mathbf{\Gamma}$ used for the MCF. $K_\nu$ is the order $\nu$ modified Bessel function of the second kind, $\sigma^2$ is related to the variance in index of refraction, and $\mathcal{L}$ is an integral length scale of the
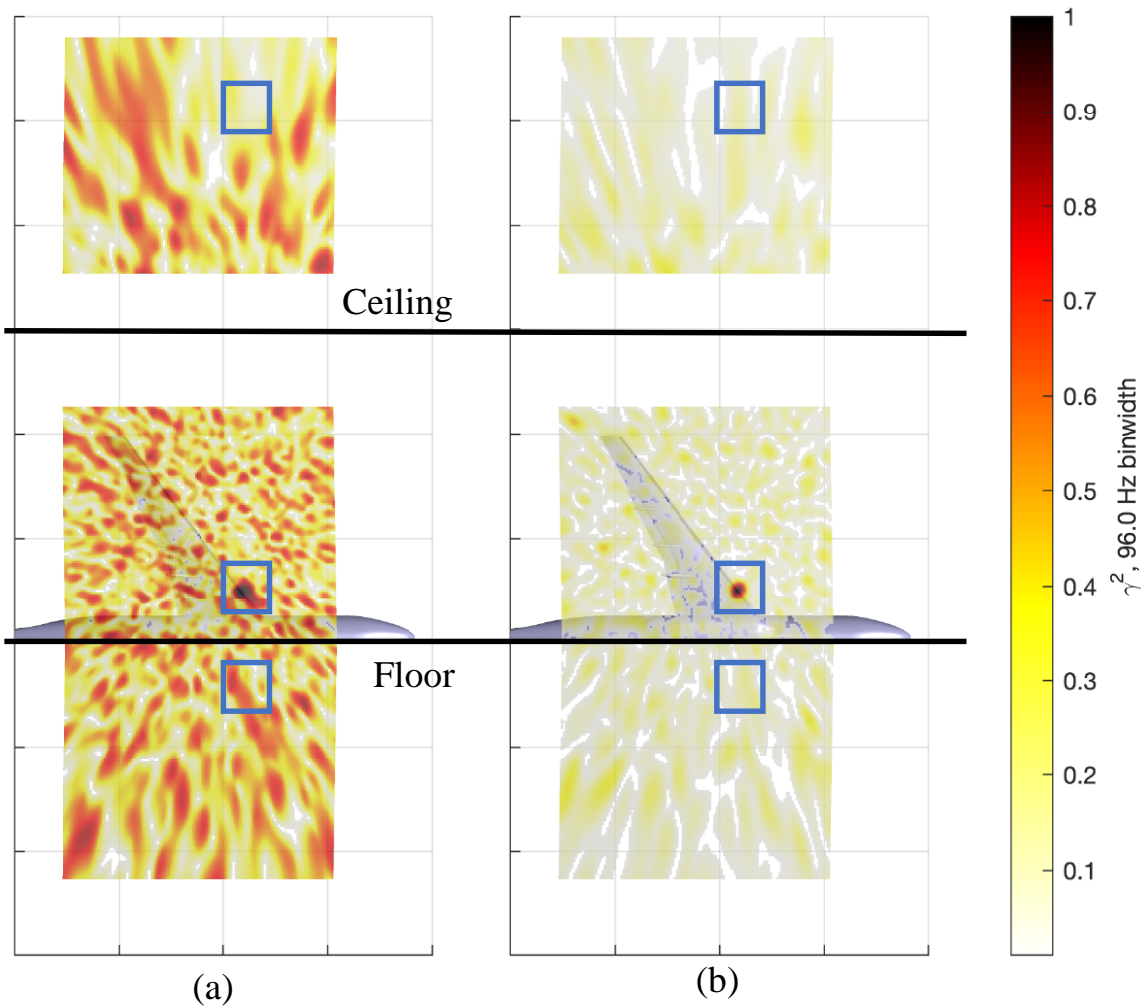
**Fig. 4** **Slat noise coherence estimates from cross-beamforming on the CRM-HL at Mach 0.2 in the closed wall test for (a) a slat tone at 8.7 kHz and (b) broadband noise at 8.0 kHz. The blue boxes encapsulate the reference grid point and its images.**

model [3]. Note that this formulation numerically fails for small arguments, but the value at zero is needed. This can be circumvented by using the asymptotic form of the modified Bessel function for small arguments and manipulating the equation, giving

$$\lim_{\rho \to 0} b_c\left(\rho\right) \approx \frac{2\sigma^2 \mathscr{L}}{3\sqrt{\pi}\Gamma\left(\frac{1}{3}\right)}\left[\Gamma\left(\frac{5}{6}\right) - \Gamma\left(\frac{1}{6}\right)\left(\frac{\rho}{2\mathscr{L}}\right)^{\frac{5}{3}}\right]. \tag{23}$$

While $\sigma^2$ and $\mathscr{L}$ are unknown, they can be determined via a nonlinear curve fit to the speaker measurement data. This is shown in Fig. 5 where the model fit is plotted over the 20 kHz coherence data from every pair of microphones in the array. For a given run condition, this fit can then be used to correct propagation from every grid point in the deconvolution domain. Note that the von Kármán fit parameters will change with a variety of test conditions and measurement locations. Speaker data were acquired at many of these conditions and locations in an attempt to build a robust model for coherence loss correction. This manuscript presents a preliminary attempt at implementing such a model using a small subset of the data. Significant improvements are expected with future work.
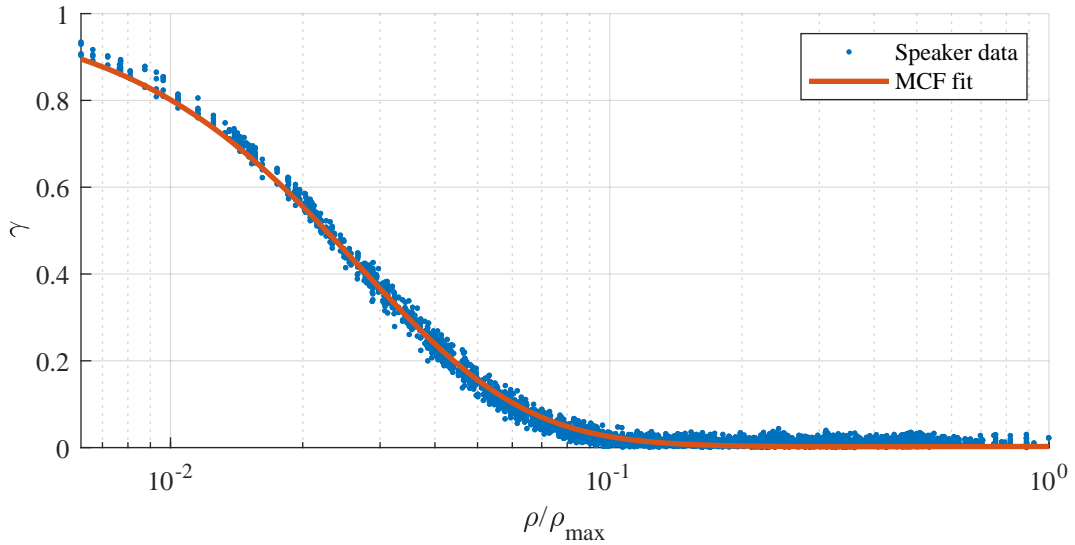


**Fig. 5** **Example fit of speaker coherence data to a von Kármán-based MCF. Data are shown at 20 kHz for Mach 0.16.**

# VI. Results

Following previous studies comparing closed and open-jet wind tunnel testing [11], processed results are compared in terms of qualitative source localization, quantitative source levels, and relative change in source levels. As this is a preliminary assessment of data, relative changes are limited to evaluating Mach number scaling of the FSS configuration, rather than comparing the FSS to the PSS and its nacelle. This avoids issues with, for example, modifying regional summation bounds to account for significant changes in model geometry.

## A. Spatial maps

One-twelfth octave band beamforming and DAMAS maps for the Mach 0.16 data are shown in Figs 6 - 9. Figure 6 shows results at 3 kHz, considered a lower frequency for the test. Figure 7 shows results at 6.7 kHz, the band with the dominant model-scale slat tone. Figure 8 shows results at 10.6 kHz, a midrange frequency. Figure 9 shows results at 30 kHz, chosen as an upper frequency for image evaluation. Beyond this, artifacts in the maps for the closed wall measurements, attributed to the perforate plate holding the screen cover on the array, become significant and detract from the intent of these comparisons.

For the 3 kHz maps shown in Fig. 6, both arrays have strong limitations due to their overall aperture and cannot localize sources very well with conventional beamforming. Beamforming concentrates energy toward the outboard

portion of the wing, but only in very broad lobes. The baseline DAMAS algorithm manages to improve localization in both tunnel configurations. Levels along the slat are overall similar, and some flap noise sources are present at similar locations in both configurations. Both models experience significant image speckle with baseline DAMAS calculations. This speckle is a characteristic of DAMAS and some other deconvolution algorithms, but tends not to occur with methods that enforce a more sparse solution [36].

Accounting for reverberance in the closed wall analysis reduces the map speckle. Accounting for coherence loss in the open-jet analysis eliminates the map speckle and improves the source localization of the DAMAS solution. Peak levels for the outboard slat noise source are different between the two, but they are also more concentrated in the open-jet map. The summed spectra results in the following section will further address these level differences. The remaining speckle in the closed wall data can be investigated by evaluating the full extent of the deconvolution grid, including the image source regions. While not shown here for the sake of brevity, the grid shows two issues. First, there is a significant amount of solution energy on the top and bottom boundaries of the grid; suggesting either that more than the initial floor and ceiling reflections may be significant, or that there are other unmodeled noise sources outside of the deconvolution domain (a source on the wall/floor or wall/ceiling junction is angularly outside of the grid). Along the latter line of reasoning, there is a significant amount of solution energy on the downstream boundary of the grid, which suggests that a large amount of tunnel acoustic noise may be contaminating the solution. CSM diagonal treatments will not eliminate this, as it is coherent across the array face. Some form of background subtraction is likely needed for further improvement of the maps of the closed wall data.

For the 6.7 kHz maps shown in Fig. 7, the results with all three kinds of processing show more similarity than they did at lower frequencies. The slat tone basically isolates to a point on the inboard region of the slat, with some variability in spread and level depending on the specifics of the processing. In the unplotted image grids for the closed wall configuration, the primary floor reflection is significant, but no boundary grid points have noticeable power.

For the 10.6 kHz maps shown in Fig. 8, the results get more complicated. With conventional beamforming, the open-jet beamforming map shows reduced resolution when compared to the closed wall map. For baseline DAMAS, the closed wall results isolate the sources as expected while showing some map speckle. The open-jet results begin to fall apart due to coherence loss. The sources are vaguely identifiable, but deconvolution provides little benefit beyond conventional beamforming. As before, incorporating image grid points reduces the speckle in the closed wall section map. Accounting for coherence loss in the open-jet processing restores DAMAS to more expected behavior, approximately matching the same source regions on the wing as seen in the closed wall map and reducing level differences. In the unplotted image grids for the closed wall configuration, source energy is found along the upper and lower grid boundaries, but not on the downstream one. This could again suggest either significant additional reflections or other tunnel noise sources vertically outside of the deconvolution domain, but noise from other parts of the tunnel circuit no longer appears to be a problem.

For the 30 kHz maps shown in Fig. 9, differences are even more stark. With the open-jet data, conventional beamforming completely fails to localize beyond a general region of energy along the midspan portion of the wing. The closed wall localization still holds reasonably well. With baseline DAMAS, the closed wall maps behave as before, isolating expected aeroacoustic sources and showing some map speckle. The open-jet map is, for the most part, unusable. As before, incorporating image grid points reduces the speckle in the closed wall map. Accounting for coherence loss in the open-jet processing restores DAMAS to more expected behavior. While individual slat brackets are not isolated as they are in the closed wall map, energy is still generally localized along the model slat. Further work on the coherence loss model is expected to improve this result. In the unplotted image grids for the closed wall configuration, source energy is found along the upper and lower grid boundaries, and has reappeared on the downstream boundary.

### B. Source quantification

Narrowband spectra of the summation regions are shown in Fig. 10. Under ideal circumstances, the closed wall and open-jet curves would match for both the wing region in Fig. 10a and the slat region in Fig. 10b. This is not the case. For the baseline curves in both cases, there is close agreement at lower frequencies. The slat tones do not match in level, though they do in frequency. The tone amplitudes show high variability for a given configuration (open-jet or closed wall), so there is little expectation that they would match across configurations. In the midrange frequency band, both the wing and slat are in close agreement until the sharp harmonic appears in the open-jet data. At high frequencies, the open-jet data diverge from the closed wall, with a noticeable change in spectral shape.

Incorporating the closed wall correction into DAMAS has little appreciable effect on the spectral levels; the overall wing level decreases by nearly one dB at high frequencies, but is an extremely close match everywhere else. Correcting

11

for coherence loss has a significant effect on the open-jet spectra. For the wing, the spectral increase is about 2 dB at high frequencies. For the slat, the spectral increase is about 5 dB. This shows the influence of undoing the smearing effect of coherence loss on localization, and its importance in getting levels for specific regions within a deconvolution map. Note that one would hope that having more physically accurate propagation modeling would help collapse the closed wall and open-jet data. Instead the improved modeling drives the curves further apart. However, one should recall that the influence of the screen cover on the closed wall data is present. As mentioned previously, this is expected to have a significant influence on overall level estimates due to its effect. It is unknown whether this is responsible for the full 8 dB difference between the corrected closed and open-jet slat spectra at 40 kHz, but such a possibility should not be excluded. The lack of background subtraction may also contribute to this discrepancy by treating model energy as a sidelobe of some peak on the beamforming grid boundary. Regardless, if these are the driving factors in this spectral difference, then one should expect that an evaluation of relative spectral differences would yield better agreement. The relative differences between Mach 0.16 and 0.2 are used to assess this premise.

## C. Relative spectral changes

Spectral difference plots for the two summation regions are shown in Fig. 11. These are plotted on a 1/12$^{\text{th}}$ octave band to smooth out the slat tone data. For this preliminary analysis, no Strouhal scaling is performed. Data in the midfrequency range are dominated by the misaligned slat tones, and thus do not give a clean statement of relative level changes. However, the low and high frequencies of the spectral differences are usable for this purpose.

At low frequencies, all of the analysis methods are nearly on top of each other at a 5 dB gain, approximately corresponding to a fifth-power Mach scaling. The complete insensitivity of the low frequency wing differences to facility and algorithm suggests that, as seen in previous studies [11], good agreement can be found between closed wall and open-jet testing for relative comparisons. There is a slight difference when the summation bounds are used to isolate the slat, where the open-jet result is slightly below the closed wall data prior to coherence correction, and slightly above afterward. These differences are small enough that they could easily be altered by adjustments to the coherence loss model.

At high frequencies, there is no difference between the baseline and image source DAMAS results for the closed wall test. This suggests that, if relative source changes for broad summation regions are the quantity of interest for a closed wall test, there is no reason to go through the computational expense of accounting for image sources with this kind of noise source. For the wing region, this is approximately flat at 6 dB gain, approximately corresponding to a sixth-power Mach scaling. There is some increase beyond this for the isolated slat region in the closed wall data, climbing above 7 dB. The open-jet results do not behave as consistently here. There is a broad ripple in the corrections from just below 20 kHz to 30 kHz. At least part of this is due to a Strouhal shift in the spectral hump visible in the narrowband plots of Fig. 10. The open-jet curves collapse at frequencies higher than this ripple for the wing difference plot but not for the slat difference plot. This shows that coherence correction plays a larger role in isolated component studies than for whole model analysis at high frequencies. For these frequencies, coherence correction brings the open-jet results closer to the closed wall results.

# VII. Summary & Future work

Microphone phased array results from two different tests of the CRM-HL in the 14x22 are presented. The tests were conducted in the closed wall and open-jet configurations of the facility test section with matching model settings and test section Mach numbers. The model AoA, while not equal between the tests, was set to approximately match static pressure distributions to compensate for the aerodynamic differences between the two tunnel configurations. These results are used to compare estimates of acoustic source strength from both the whole CRM-HL wing and the leading edge slat.

Conventional beamforming images show qualitative agreement at low to mid frequencies, though the closed wall data suffer from background noise contamination for lower frequency maps. At high frequencies, coherence loss due to the open-jet shear layer makes source localization difficult with the open-jet data. Baseline DAMAS results, where the DAMAS algorithm's coefficient matrix is computed with the traditional models, trend similarly. Background contamination and reverberance contaminate the DAMAS output with speckled maps for the closed wall results. For increasing frequency, coherence loss eventually smears the open-jet DAMAS output to the point of near-uselessness. Incorporating primary image sources into the closed wall DAMAS analysis reduces, but does not eliminate, map speckle. Incorporating coherence loss into the open-jet DAMAS analysis dramatically improves source localization, allowing

12

summed source analysis.

For quantitative spectra, the use of the baseline DAMAS algorithm yields reasonable agreement between the two tunnel configurations at low to midfrequencies. Divergence begins at high frequencies where the spectral shapes differ. Counterintuitively, improving the physics modeling in the propagation functions is detrimental to the agreement between the two facility configurations. This may be explained by the lack of consideration given to the effect of the protective screen cover used in the closed wall configuration, as well as the lack of a background noise reference.

For relative spectral comparisons, the choice of DAMAS propagation model makes no difference for the closed wall test. It matters somewhat for the open-jet data, but the differences are far less significant than with quantitative spectra. All methods are in extremely close agreement for lower frequencies. Further scaling analysis is required for higher frequencies.

Overall, correcting the closed wall DAMAS analysis with image sources plays a minor role in generating cleaner deconvolution maps, but does little else. The quantitative changes from this correction are miniscule, and are likely dwarfed by the possible improvements from correcting for the array cover screen and having background data to subtract. Correcting the open-jet DAMAS analysis for coherence loss plays a significant role in generating deconvolution maps which allow for source interpretation, though further model development is required. The quantitative changes from this correction are also significant. This current study has not finalized the corrections necessary to collapse closed wall and open-jet microphone phased array results, but it has identified the next steps.

Future closed wall tests should include empty tunnel acquisitions in the plan whenever possible. Also, detailed quantification of the influence of any instrumentation covers would be helpful should quantitative spectra be desired. Alternatively, other means of keeping the wall turbulent boundary layer off acoustic instrumentation should be considered. Future open-jet tests should always include test points that allow for the development of a coherence loss model. This will require the use of known acoustic sources to interrogate the open-jet shear layer and/or detailed flow measurements to include in a coherence loss model. The proper application of these models to deconvolution routines is also ripe for future study, as the current work only represents a preliminary pass at the technique.
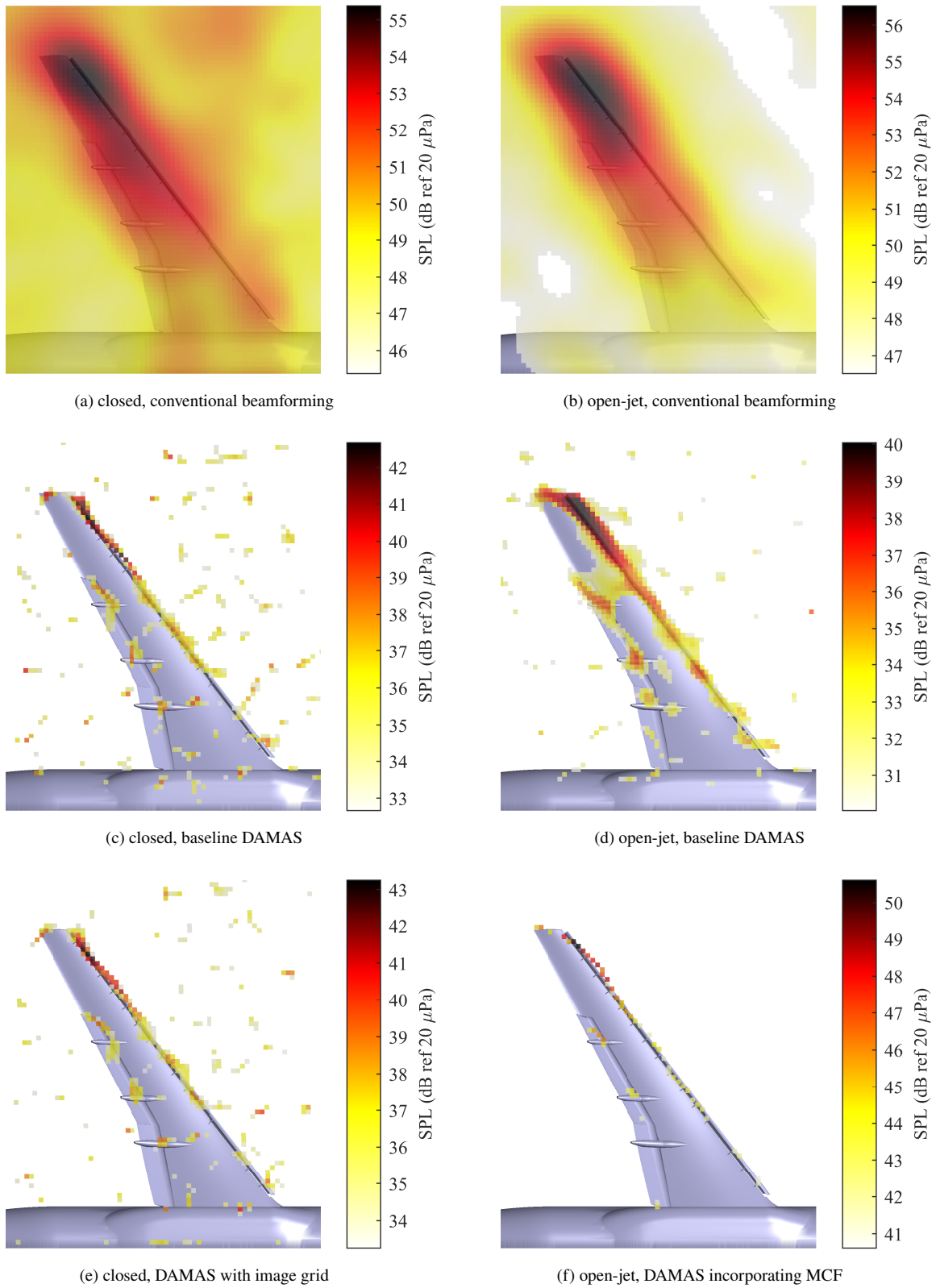
## Acknowledgments

## References

[1] Soderman, P. T., and Allen, C. S., "Microphone Measurements In and Out of Airstream," *Aeroacoustic Measurements*, edited by T. J. Mueller, Springer-Verlag, Berlin, Heidelberg, New York, 2002, pp. 1 – 61.

[2] Devenport, W. J., Burdisso, R. A., Borgoltz, A., Ravetta, P. A., Barone, M. F., Brown, K. A., and Morton, M. A., "The Kevlar-walled anechoic wind tunnel," *Journal of Sound and Vibration*, Vol. 332, No. 17, 2013, pp. 3971 – 3991.

[3] Dougherty, R. P., "Turbulent Decorrelation of Aeroacoustic Phased Arrays: Lessons from Atmospheric Science and Astronomy," *9th AIAA/CEAS Aeroacoustics Conference*, AIAA 2003-3200, Hilton Head, South Carolina, 12 – 14 May 2003.

[4] Bahr, C. J., Hutcheson, F. V., and Stead, D. J., "Assessment of Unsteady Propagation Characteristics and Corrections in Aeroacoustic Wind Tunnels Using an Acoustic Pulse," *24th AIAA/CEAS Aeroacoustics Conference*, AIAA 2018-3118, Atlanta, Georgia, 25 – 29 June 2018.

[5] Ahlefeldt, T., "Microphone Array Measurement in European Transonic Wind Tunnel at Flight Reynolds Numbers," *AIAA Journal*, Vol. 55, No. 1, 2017, pp. 36 – 48.

[6] Guidati, S., Brauer, C., and Wagner, S., "The Reflection Canceller - Phased Array Measurements in a Reverberating Environment," *8th AIAA/CEAS Aeroacoustics Conference*, AIAA 2002-2464, Breckenridge, Colorado, 17 – 19 June 2002.

[7] Fischer, J., and Doolan, C., "Beamforming in a reverberant environment using numerical and experimental steering vector formulations," *Mechanical Systems and Signal Processing*, Vol. 91, 2017, pp. 10 – 22.
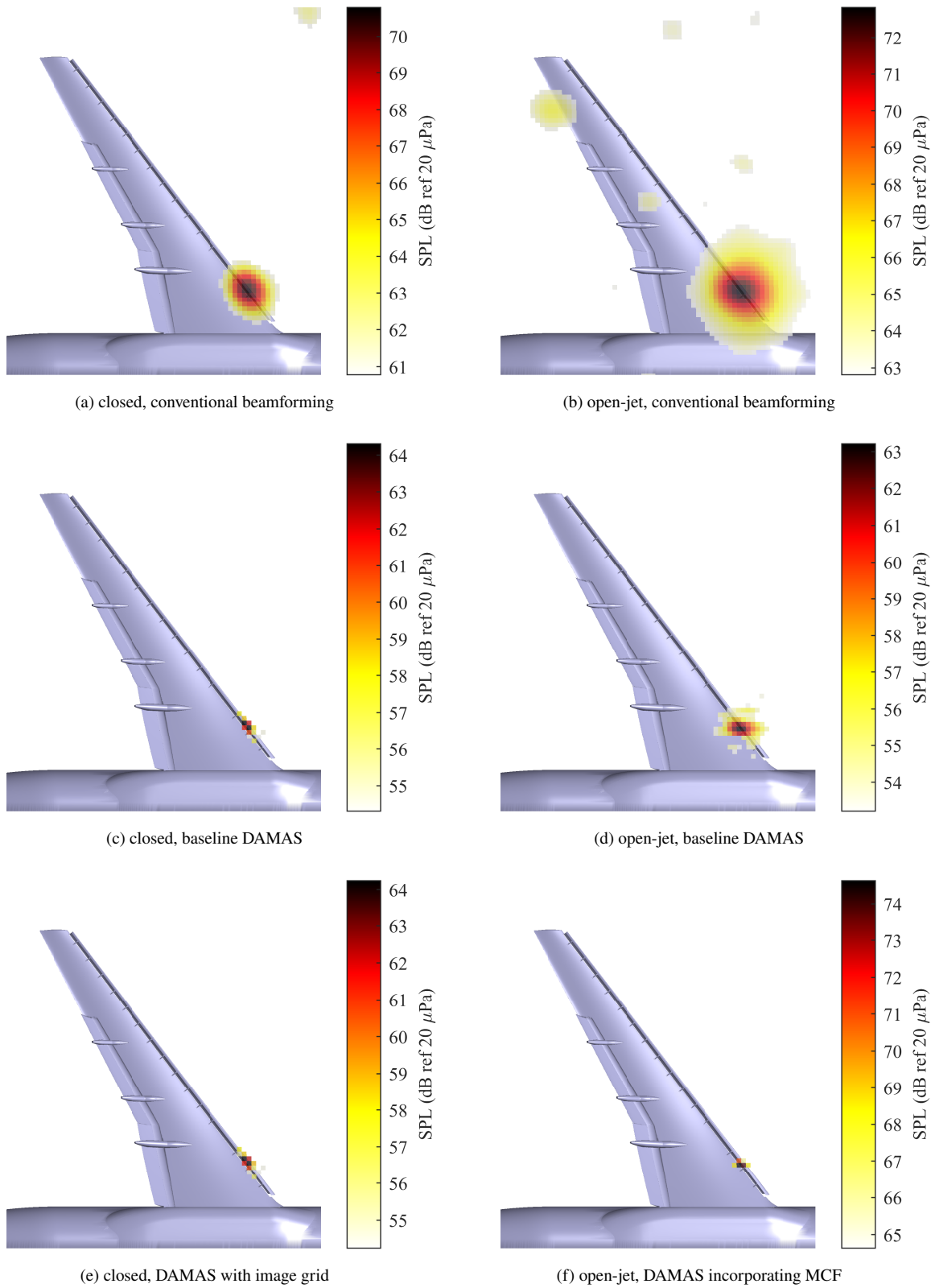
[8] Sijtsma, P., and Holthusen, H., "Corrections for Mirror Sources in Phased Array Processing Techniques," *9th AIAA/CEAS Aeroacoustics Conference*, AIAA 2003-3196, Hilton Head, South Carolina, 12 – 14 May 2003.

[9] Fenech, B. A., and Takeda, K., "Towards More Accurate Beamforming Levels in Closed-Section Wind Tunnels via De-Reverberation," *13th AIAA/CEAS Aeroacoustics Conference*, AIAA 2007-3431, Rome, Italy, 21 – 23 May 2007.

[10] Bahr, C. J., "Deconvolution in Reverberant Wind Tunnels: A DAMAS Study," *26th AIAA/CEAS Aeroacoustics Conference*, presentation only, 15 – 19 June 2020.

[11] Oerlemans, S., Broersma, L., and Sijtsma, P., "Quantification of airframe noise using microphone arrays in open and closed wind tunnels," *International Journal of Aeroacoustics*, Vol. 6, No. 4, 2007, pp. 309 – 333.

[12] Lockard, D. P., Turner, T. L., Bahr, C. J., and Hutcheson, F. V., "Overview of Aeroacoustic Testing of the High-Lift Common Research Model," *27th AIAA/CEAS Aeroacoustics Conference*, to be published, 2 – 6 August 2021.

[13] Brooks, T. F., and Humphreys, W. M., "A deconvolution approach for the mapping of acoustic sources (DAMAS) determined from phased microphone arrays," *Journal of Sound and Vibration*, Vol. 294, 2006, pp. 856 – 879.

[14] Merino-Martínez, R., Sijtsma, P., Snellen, M., Ahlefeldt, T., Antoni, J., Bahr, C. J., Blacodon, D., Ernst, D., Finez, A., Funke, S., Geyer, T. F., Haxter, S., Herold, G., Huang, X., Humphreys, W. M., Leclère, Q., Malgoezar, A., Michel, U., Padois, T., Pereira, A., Picard, C., Sarradj, E., Siller, H., Simons, D. G., and Spehr, C., "A review of acoustic imaging methods using phased microphone arrays," *CEAS Aeronautical Journal*, Vol. 10, No. 1, 2019, pp. 197 – 230.

[15] Papamoschou, D., and Mayoral, S., "Modeling of Jet Noise Sources and their Diffraction with Uniform Flow," *51st AIAA Aerospace Sciences Meeting*, AIAA 2013-0326, Grapevine, Texas, 7 – 10 January 2013.

[16] Sarradj, E., "Three-Dimensional Acoustic Source Mapping with Different Beamforming Steering Vector Formulations," *Advances in Acoustics and Vibration*, Vol. 2012, No. 292695, 2012, pp. 1 – 12.

[17] Johnson, D. H., and Dudgeon, D. E., *Array Signal Processing: Concepts and Techniques*, Prentice Hall, Upper Saddle River, NJ, 1993, Chap. 4.

[18] Dougherty, R. P., "Beamforming in Acoustic Testing," *Aeroacoustic Measurements*, edited by T. J. Mueller, Springer-Verlag, Berlin, Heidelberg, New York, 2002, pp. 62 – 97.

[19] Ehrenfried, K., and Koop, L., "Comparison of Iterative Deconvolution Algorithms for the Mapping of Acoustic Sources," *AIAA Journal*, Vol. 45, No. 7, 2007, pp. 1584 – 1595.

[20] Chardon, G., Picheral, J., and Ollivier, F., "Theoretical analysis of the DAMAS algorithm and efficient implementation of the covariance matrix fitting method for large-scale problems," *Journal of Sound and Vibration*, Vol. 508, 2021, pp. 1 – 15.

[21] Ostashev, V. E., and Wilson, D. K., "Strength and wave parameters for sound propagation in random media," *The Journal of the Acoustical Society of America*, Vol. 141, No. 3, 2017, pp. 2079 – 2092.

[22] Wilson, D. K., "Performance bounds for acoustic direction-of-arrival arrays operating in atmospheric turbulence," *The Journal of the Acoustical Society of America*, Vol. 103, No. 3, 1998, pp. 1306 – 1319.

[23] Koop, L., Ehrenfried, K., and Kröber, S., "Investigation of the systematic phase mismatch in microphone-array analysis," *11th AIAA/CEAS Aeroacoustics Conference*, AIAA 2005-2962, Monterey, California, 23 – 25 May 2005.

[24] Sijtsma, P., "Acoustic array corrections for coherence loss due to the wind tunnel shear layer," Tech. Rep. NLR-TP-2008-112, NLR, February 2008.

[25] Ernst, D., Spehr, C., and Berkefeld, T., "Decorrelation of Acoustic Wave Propagation through the Shear Layer in Open Jet Wind Tunnel," *21st AIAA/CEAS Aeroacoustics Conference*, AIAA 2015-2976, Dallas, Texas, 22 – 26 June 2015.

[26] Lockard, D. P., O'Connell, M. D., Vatsa, V. N., and Choudhari, M. M., "Assessment of Aeroacoustic Simulations of the High-Lift Common Research Model," *25th AIAA/CEAS Aeroacoustics Conference*, Delft, The Netherlands, 20 – 23 May 2019.

[27] Horne, W. C., Burnside, N. J., Schery, S. D., Podboy, G. G., Bahr, C. J., Stead, D. J., and Humphreys, W. M., "Effects of resistive windscreens and foam inserts on the acoustic response of an in-flow phased microphone array," *AIAA SciTech Forum*, AIAA 2021-0217, 19 – 21 January 2021.

[28] Humphreys, W. M., Brooks, T. F., Bahr, C. J., Spalt, T. B., Bartram, S. M., and Culliton, W. G., "Development of A Microphone Phased Array Capaability for the Langley 14- by 22-Foot Subsonic Tunnel," *20th AIAA/CEAS Aeroacoustics Conference*, AIAA 2014-2343, Atlanta, Georgia, 16 – 20 June 2014.

[29] Hald, J., "Removal of incoherent noise from an averaged cross-spectral matrix," *The Journal of the Acoustical Society of America*, Vol. 142, No. 2, 2017, pp. 846 – 854.

[30] Bahr, C. J., and Horne, W. C., "Subspace-based background subtraction applied to aeroacoustic wind tunnel testing," *International Journal of Aeroacoustics*, Vol. 16, No. 4 & 5, 2017, pp. 299 – 325.

[31] Amiet, R. K., "Refraction of Sound by a Shear Layer," *Journal of Sound and Vibration*, Vol. 58, No. 4, 1978, pp. 467 – 482.

[32] Bahr, C. J., and Lockard, D. P., "Designing Shading Schemes for Microphone Phased Arrays," *8th Berlin Beamforming Conference*, BeBeC-2020-S1, Berlin, Germany, 2 – 3 March 2020.

[33] *Method for Calculation of the Absorption of Sound by the Atmosphere*, ANSI S1.26-1995 (ASA 113-1995), Acoustical Society of America, 1995.

[34] Bahr, C. J., Brooks, T. F., Humphreys, W. M., Spalt, T. B., and Stead, D. J., "Acoustic Data Processing and Transient Signal Analysis for the Hybrid Wing Body 14- by 22-Foot Subsonic Wind Tunnel Test," *20th AIAA/CEAS Aeroacoustics Conference*, AIAA 2014-2345, Atlanta, Georgia, 16 – 20 June 2014.

[35] Brooks, T. F., and Humphreys, W. M., "Extension of DAMAS Phased Array Processing for Spatial Coherence Determination (DAMAS-C)," *12th AIAA/CEAS Aeroacoustics Conference*, AIAA 2006-2654, Cambridge, Massachusetts, 8 – 10 May 2006.

[36] Bahr, C. J., Humphreys, W. M., Ernst, D., Ahlefeldt, T., Spehr, C., Pereira, A., Leclère, Q., Picard, C., Porteous, R., Moreau, D. J., Fischer, J., and Doolan, C. J., "A Comparison of Microphone Phased Array Methods Applied to the Study of Airframe Noise in Wind Tunnel Testing," *23rd AIAA/CEAS Aeroacoustics Conference*, AIAA 2017-3718, Denver, Colorado, 5 – 9 June 2017.
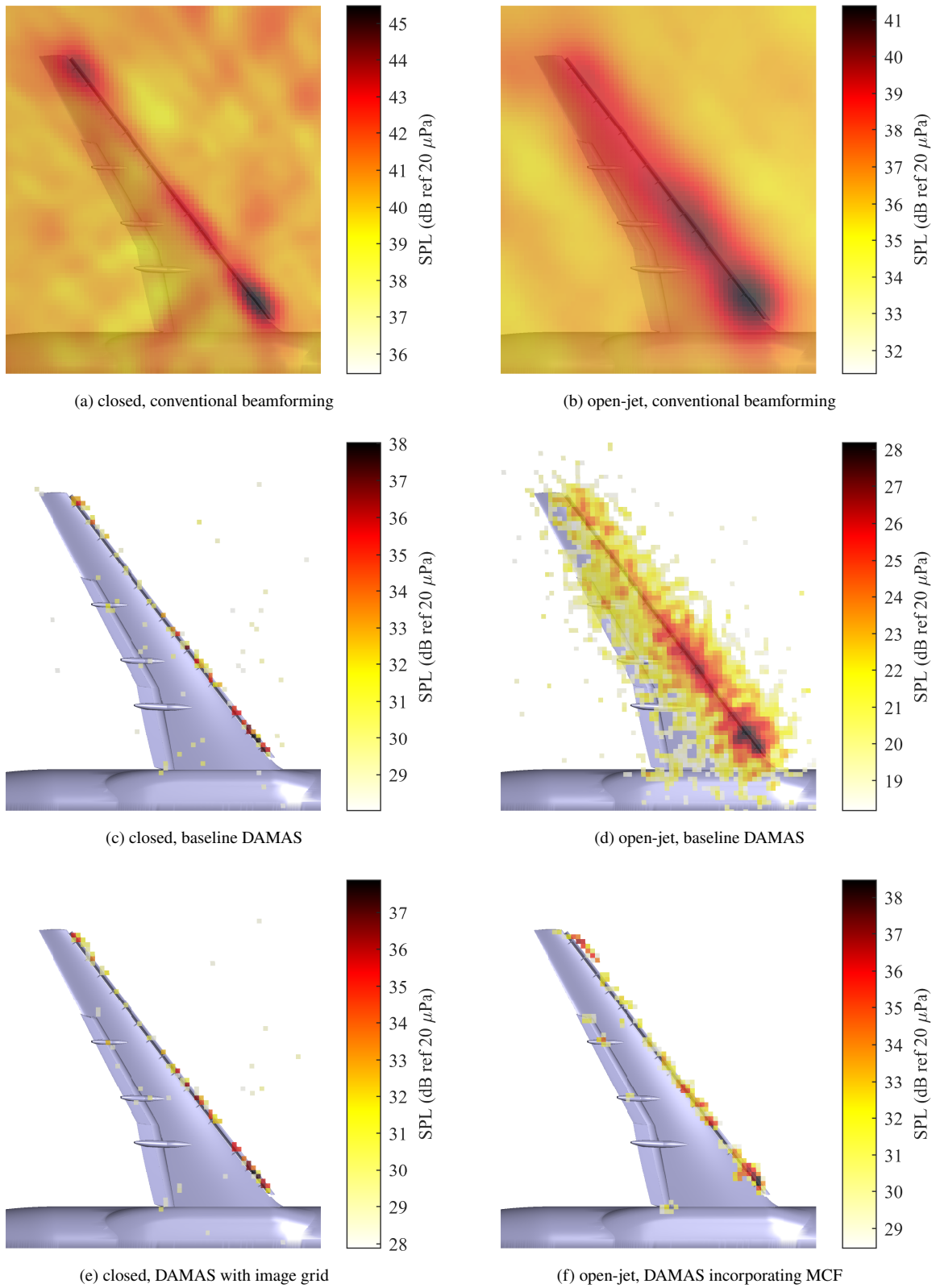
(a) closed, conventional beamforming

(b) open-jet, conventional beamforming

(c) closed, baseline DAMAS

(d) open-jet, baseline DAMAS

(e) closed, DAMAS with image grid

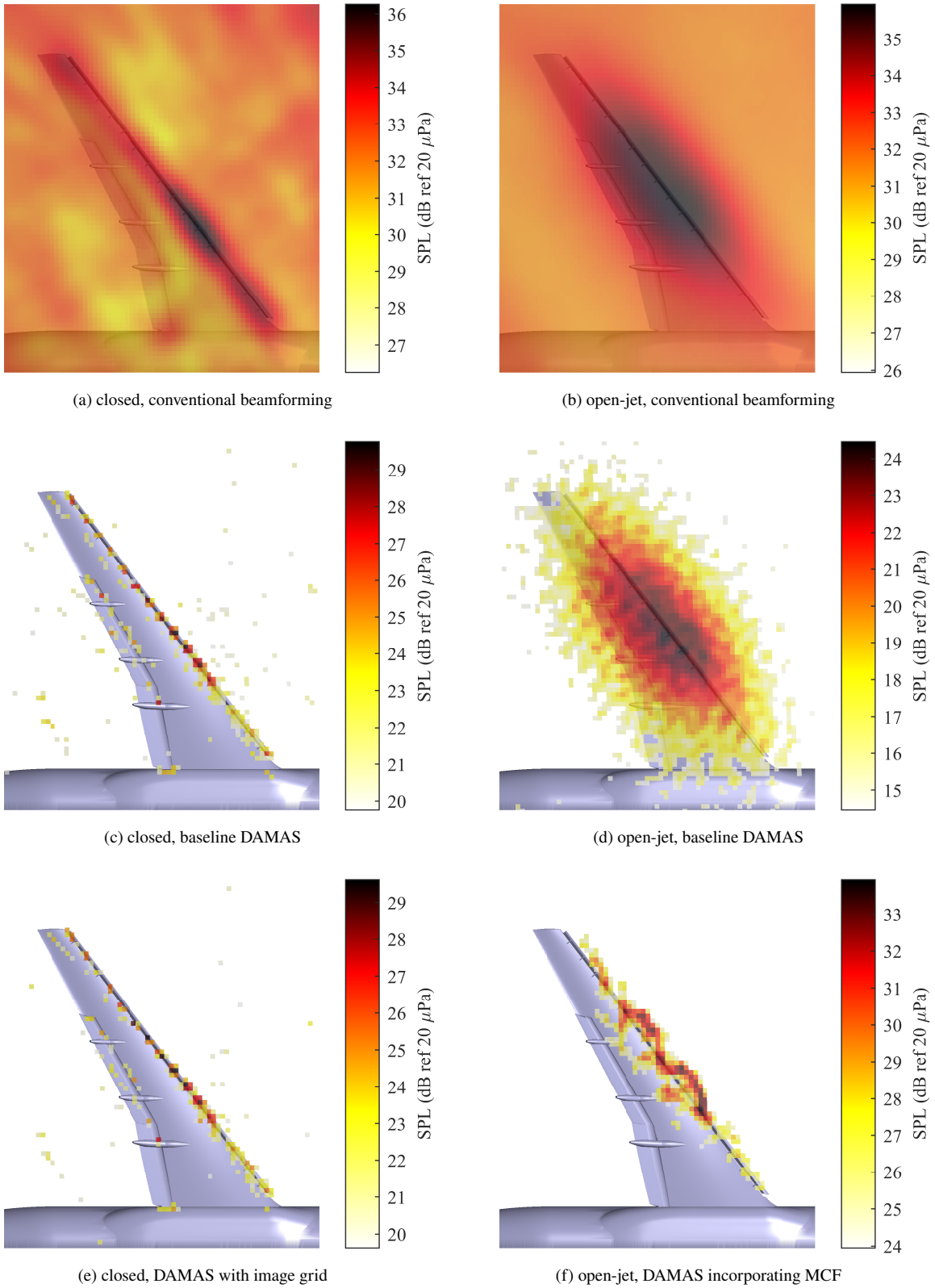(f) open-jet, DAMAS incorporating MCF

**Fig. 6    Comparison of noise source maps for the 3 kHz /12$^{th}$ octave band at Mach 0.16.**

(a) closed, conventional beamforming

(b) open-jet, conventional beamforming

(c) closed, baseline DAMAS

(d) open-jet, baseline DAMAS

(e) closed, DAMAS with image grid

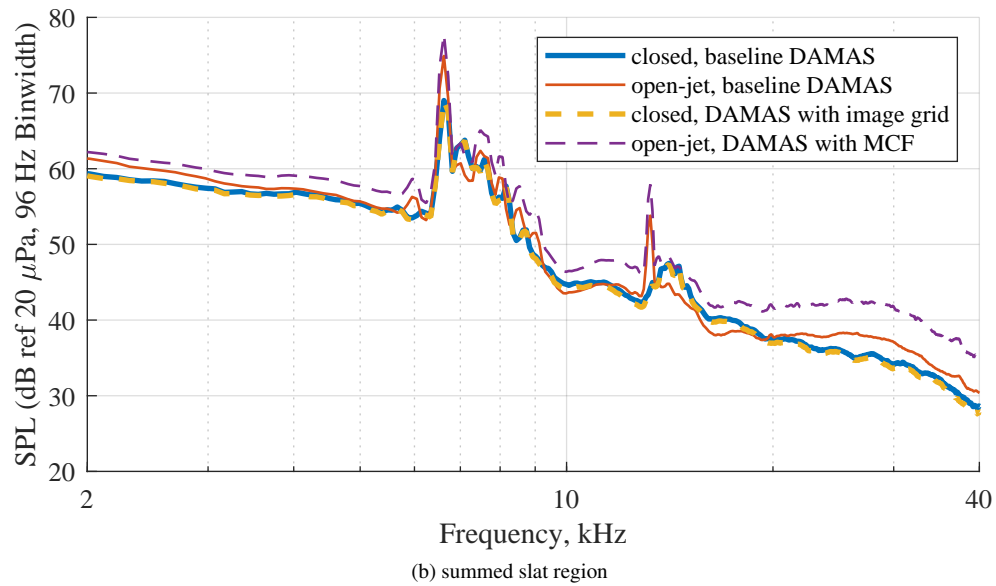(f) open-jet, DAMAS incorporating MCF

**Fig. 7    Comparison of noise source maps for the 6.7 kHz /12$^{th}$ octave band at Mach 0.16.**

(a) closed, conventional beamforming

(b) open-jet, conventional beamforming

(c) closed, baseline DAMAS

(d) open-jet, baseline DAMAS

(e) closed, DAMAS with image grid

(f) open-jet, DAMAS incorporating MCF

**Fig. 8   Comparison of noise source maps for the 10.6 kHz /12$^{\text{th}}$ octave band at Mach 0.16.**

(a) closed, conventional beamforming

(b) open-jet, conventional beamforming

(c) closed, baseline DAMAS

(d) open-jet, baseline DAMAS

(e) closed, DAMAS with image grid

(f) open-jet, DAMAS incorporating MCF

**Fig. 9    Comparison of noise source maps for the 30 kHz /12$^{th}$ octave band at Mach 0.16.**

(a) summed wing region



(b) summed slat region
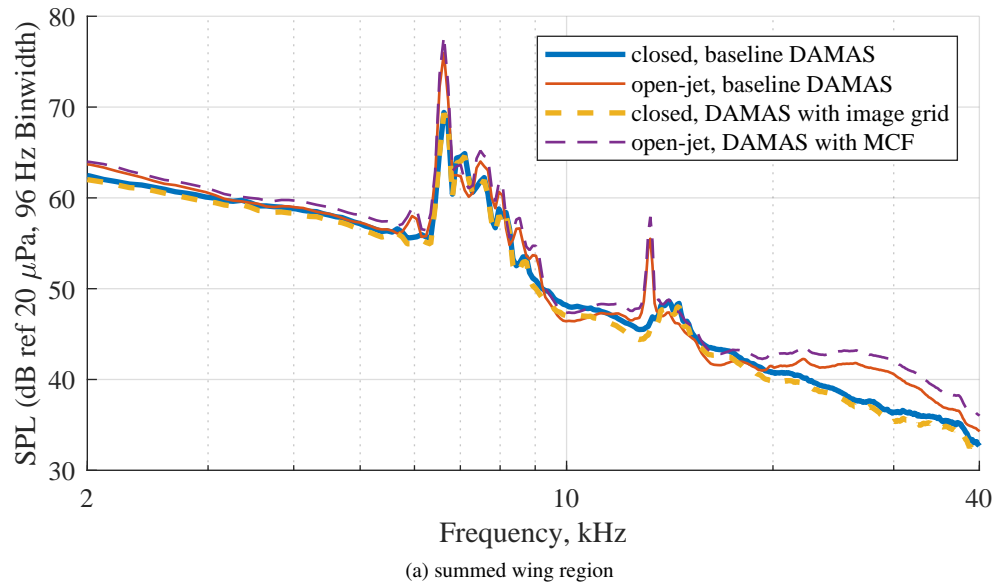
**Fig. 10    Comparison of summed source region narrowband spectra at Mach 0.16.**

(a) summed wing region



(b) summed slat region
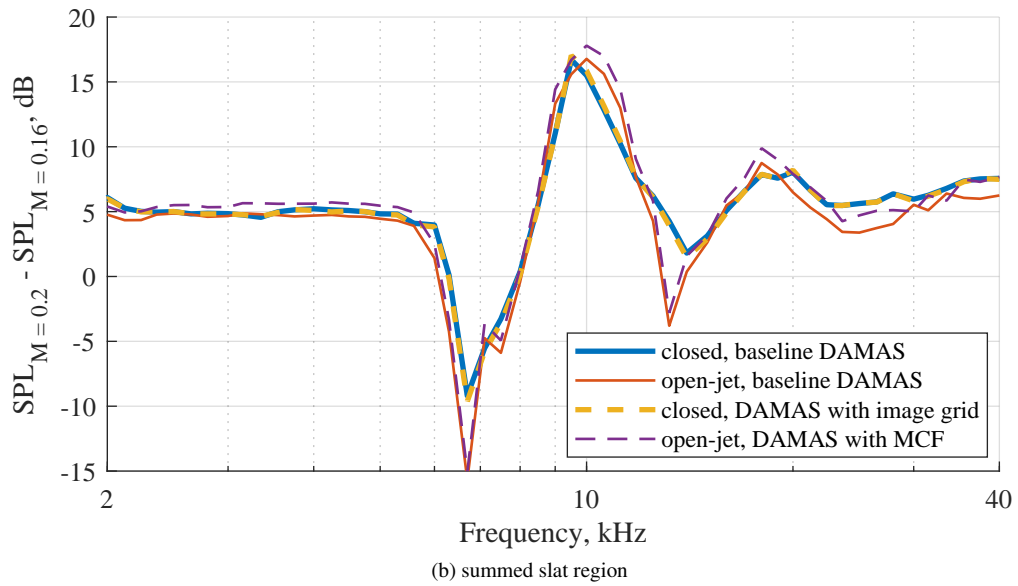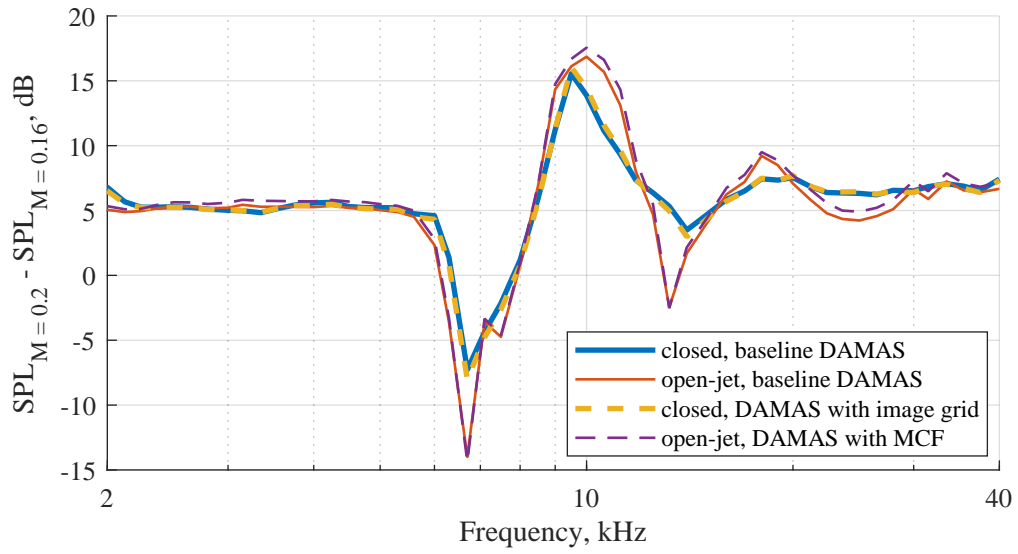
**Fig. 11   Comparison of 1/12$^{\text{th}}$ octave band spectral differences between Mach 0.2 and Mach 0.16.**